JGR Atmospheres

RESEARCH ARTICLE
10.1029/2020JD033601

Special Section:
Atmospheric PM2.5 in China: physics, chemistry, measurements, and modeling

Aerosol-Radiation Interactions of Dust Storm Deteriorate Particle and Ozone Pollution in East China

Zilin Wang[1,2], Xin Huang[1,2], Nan Wang[1,2,3], Jiawei Xu[1,2], and Aijun Ding[1,2]

[1]Joint International Research Laboratory of Atmospheric and Earth System Sciences, School of Atmospheric Sciences, Nanjing University, Nanjing, China, [2]Jiangsu Provincal Collorative Innovation Center of Climate Change, Nanjing, China, [3]Institute of Tropical and Marine Meteorology, China Meteorological Administration, Guangzhou, China

Abstract East Asia features frequent dust storms and intensive anthropogenic emissions. The mixing of natural dust and anthropogenic pollutants exerts complicated impacts on air pollution and regional climate. Studies have focused on chemical interactions of the mixed pollution, while the meteorological feedback and influences on atmospheric chemistry have not been fully investigated. Here, a comprehensive study on a widespread dust storm and its influence on the air quality downwind was conducted by combining multiple observations and modeling. We found that dust originated from Gobi Desert was mixed with anthropogenic pollutants after transported to the Yangtze River Delta (YRD). Through scattering and absorbing radiation, dust aerosol perturbed solar energy budget and led to a more stabilized planetary boundary layer (PBL). A reduction of 15% in PBL height (184 m) weakened the dispersion of locally emitted pollutants and increased primary pollution by 10% in YRD city clusters. Besides, the mixed plume over offshore areas warmed the entire lower atmosphere and increased surface evaporation. Accordingly, ozone formation was accelerated by ~1 ppbv/h within PBL under higher temperature, and secondary aerosol was increased due to faster photochemical and heterogeneous oxidation. Such enhancements substantially contributed to air quality deterioration in YRD region. This work reveals the complexity of interactions between natural dust and anthropogenic pollutants through both atmospheric chemistry and meteorological feedbacks, which is of great importance in both regional air pollution and climate.

Key Points:

- Natural dust mixed with anthropogenic aerosols exerted great interactions with radiation and meteorology
- Dust-induced aerosol-radiation interactions over land enhanced the pollution accumulation
- Formation of ozone and secondary aerosols over ocean was promoted by aerosol-radiation interactions

Supporting Information:

- Supporting Information S1

Correspondence to:
X. Huang,
xinhuang@nju.edu.cn

Citation:
Wang, Z., Huang, X., Wang, N., Xu, J., & Ding, A. (2020). Aerosol-radiation interactions of dust storm deteriorate particle and ozone pollution in East China. *Journal of Geophysical Research: Atmospheres*, *125*, e2020JD033601. https://doi.org/10.1029/2020JD033601

Received 27 JUL 2020
Accepted 1 NOV 2020

© 2020. American Geophysical Union. All Rights Reserved.

1. Introduction

Mineral dust is recognized as one of the most important aerosol species in the troposphere. High loadings of dust particles could severely impair the visibility, disrupt social and economic activities and pose a hazardous effect to human health, such as raising the risk of respiratory disease (K. H. Kim et al., 2013; Shiraiwa et al., 2017). After its deposition to the earth surface, dust may also participate in global biogeochemical cycle by acting as a potential source of essential nutrients to marine and terrestrial ecosystems (Mahowald et al., 2005), or lower the albedo of snow/ice surface as dark impurities (Painter et al., 2007). Intense dust storm frequently hits eastern Asia under the influence of subtropical cyclones and frontal systems (Husar et al., 2001; J. Kim, 2008). Exerting great impact on dense population and concentrated human activities, dust storm stands as a prominent and outstanding problem over this area (J. Huang et al., 2014). Annually, about 800 Tg of dust over East Asia is injected into the atmosphere, 50% of which can be transported to downstream areas such as eastern China, Korea, Japan, and even Pacific Ocean by large-scale meteorological processes, leading to widespread dust events lasting for several days (Chun et al., 2001; Shao & Dong, 2006; X. Wang et al., 2004).

As one of the absorbing aerosols, mineral dust has been the focus of tremendous studies owing to its critical interaction with radiation and clouds. The radiative forcing of dust aerosol was investigated by online coupled meteorology-chemistry model, which exhibits a negative forcing at ground surface and positive in the atmosphere (L. Liu et al., 2016). The heating rate induced by dust was estimated using radiative transfer model along with satellite observations and can reach as high as 5.5 K/day in the mid troposphere (J. Huang et al., 2009). Moreover, dust aerosol was reported positively correlated with precipitation over central India, which is attributed to enhanced Indian summer monsoon and moisture transport caused by dust heating over Arabian Sea (Vinoj et al., 2014). Indirectly, droplet size distribution and coverage of shallow water clouds are significantly influenced by mineral dust as indicated by statistical analysis over subtropical arid

areas (Kaufman et al., 2005). In parallel to the aforementioned effect, absorbing aerosol is also proved to be related to enhanced haze pollution through increasing atmospheric stability or stagnation, which is found both in regional and global models considering effect of aerosols (A. J. Ding et al., 2016; X. Huang, Ding, Wang, et al., 2020; Lou et al., 2019; Z. Wang, Huang, & Ding, 2018). However, most of them focused on black carbon from anthropogenic emissions and the role of natural absorbing aerosol like dust is scarcely explored and quantified. Together with its substantial emission, Asian dust may exert a significant impact on tropospheric meteorology and air quality over both the source region and downstream areas.

Located at the eastern edge of Continental Asia, Yangtze River Delta (YRD) is one of the most rapidly developing regions with large energy consumption. Although declined trends of anthropogenic emissions have been verified in up-to-date studies (Gu et al., 2013; Zheng et al., 2018), the magnitude of gaseous and aerosol pollutants is still high compared to their counterparts in other city clusters worldwide. In fact, particulate matter and ozone pollution could be frequently observed in this region due to high intensity of human activities (Fu et al., 2008; L. Li et al., 2011). Besides, YRD also suffers from long-range transported mineral dust from inland source regions such as Gobi Desert, which is often mixed with anthropogenic pollutants (X. X. Zhang et al., 2018; Zhou et al., 2018). Such mixing can contribute to the deterioration of air quality in two ways. First, high levels of acid gaseous precursors such as sulfur dioxide (SO_2) and nitrogen dioxide (NO_2) were taken in by dust particle, leading to the formation of sulfate and nitrate aerosols via heterogeneous reactions (Jordan et al., 2003; J. Li et al., 2012; Q. Wang, Dong, et al., 2018). In some other cases, the formation and growth rate of small particles were observed to be enhanced under the influence of photo-induced, dust surface-mediated reactions during a polluted dust (Nie et al., 2014). Second, the positive feedback between dust and boundary layer stability may enhance the local pollution, which becomes more prominent as the absorbing efficiency of dust was significantly enhanced after mixed with anthropogenic aerosols (Obregón et al., 2015; Tian et al., 2018).

In this study, a widespread dust event as well as its influence on air quality of downstream cities was thoroughly analyzed using observations combined with regional air quality modeling. The dust originated from Gobi Desert was first transported southwards to YRD city clusters, worsening the ventilation conditions and exacerbating the local-emitted primary pollution. Then, the plume was exported to East China Sea, where the secondary pollution was invigorated and finally recirculated back to YRD, raising the concentration of ozone and secondary inorganic aerosols in coastal cities. The mixing of natural dust and anthropogenic pollutants is one of the major issues which can severely damage the air quality and ecosystem through chemical reactions and meteorological feedback. The latter process could be more pronounced considering the amplification of dust absorbing properties after mixing. Therefore, the study aims to improve our understandings on the mixed pollution induced aerosol-radiation interaction and its influence on regional environment. The rest of the article is organized as follows. The observational data and methodology are introduced in Section 2. Section 3 consists of the overview of this dust event as well as model evaluation, the impact of dust-induced aerosol-radiation interaction (ARI) on primary pollution accumulation and secondary pollution formation. Conclusions are summarized in Section 4.

2. Data and Method

2.1. Ground-Based and Satellite Observations

Hourly ground-level meteorological variables (including 2m-temperature, relative humidity, wind speed and direction, etc.) archived at the US National Climate Data Center (NCDC), and hourly concentrations of $PM_{2.5}$, PM_{10}, and ozone released by the Ministry of Ecology and Environment of China were collected through October to November 2019 to picture the evolvement of the pollution episode and perform evaluation for the model. Primary and secondary aerosols including their chemical composition and radiative flux at the Stations for Observing Regional Processes of the Earth System (SORPES) in Nanjing were routinely recorded. The concentrations of sulfate, nitrate, and ammonium and other water-soluble ions were measured using the Monitor for Aerosols and Gases in Ambient Air. Radiation and heat flux were observed by flux measurement system mounted on a 3-m tower at the station. Detailed description of the site and instruments could be found in A. Ding, Huang, et al. (2019). Atmospheric sounding at Nanjing (32.00°N, 118.80°E, WMO station number 58238) has also been applied to compare with temperature profile provided by global forecast system. The radiosondes were launched twice a day (00:00 and 12:00 UTC) to detect

Table 1
WRF-Chem Domain Setting and Configurations for Physical/Chemical Parameterization

Domain setting	
Horizontal grid	181 × 201 (20 km)
Vertical layers	40
Model configuration	
Shortwave radiation	RRTMG
Longwave radiation	RRTMG
Land surface	Noah
Surface layer	Monin-Obukhov
Boundary layer	YSU
Microphysics	Lin et al.
Cumulus parameterization	Grell-Deveny
Photolysis	Fast-J
Gas-phase and aerosol chemistry	CBMZ and MOSAIC

Abbreviations: CBMZ, Carbon Bond Mechanism version Z; MOSAIC, Model for Simulating Aerosol Interactions and Chemistry; RRTMG, rapid radiative transfer model.

atmospheric variables (air temperature, wind speed, water mixing ratio, etc.) on primarily mandatory pressure levels for the lower troposphere.

Satellite-retrieved aerosol optical depth (AOD) at mid-visible channel (550 nm) provided by MODerate resolution Imaging Spectroradiometer (MODIS Collection 6.1) with a horizontal resolution of 10 km (MOD04, Terra) was applied to show general information of the dust storm. In addition, the Level 2 aerosol profile and vertical feature mask from the Cloud-Aerosol Lidar and Infrared Pathfinder Satellite Observation (CALIPSO version 4) datasets were used to provide information of vertical distribution and transport of dust aerosols.

2.2. Regional Meteorology-Chemistry Coupled Modeling

Numerical simulations of meteorological and chemical processes during the episode are conducted by WRF-Chem version 4.0, which is an online-coupled three-dimensional transport model considering source and emission of pollutants, gas-phase and aqueous chemical transformations, aerosol dynamics, and deposition (Grell et al., 2005). The model also describes direct and indirect effect of aerosols, and has been widely applied to study the aerosol's feedback on radiation and clouds (A. J. Ding et al., 2016; X. Huang et al., 2016). The model domain covered the entire eastern China and surrounding areas with a 20 × 20 km grid resolution. Vertically, 40 layers extended from the ground surface to the model top (50 hPa), with more levels placed in the lower troposphere to better describe boundary layer processes. To investigate the dust transport and subsequent pollution in YRD, the simulation was operated for 2 weeks from mid-October to early November, leaving the first 5 days as spin-up. For each day a run covering 36 h was conducted and the last 24-h results are analyzed to minimize the influence of initial conditions and retain thermodynamic effects of aerosols (Berge et al., 2001; A. J. Ding et al., 2016). The initial and boundary conditions of meteorological variables are obtained from National Center for Environment Prediction (NCEP) global final analysis data (FNL) with a 1° × 1° spatial resolution that update every 6 h. For chemical fields such as ozone, the initial and lateral boundary conditions are based on prescribed vertical profile as those of McKeen (2002). The outputs of chemical species from previous runs were used as the initial conditions for the following run.

Table 1 summarizes the selected physical and chemical options for WRF-Chem, which have been successfully adopted in our previous work on ARI. A new version of the rapid radiative transfer model was utilized to simulate the radiation transfer procedure for both shortwave and longwave radiation within the atmosphere (Iacono et al., 2008; Zhao et al., 2011). Noah land surface scheme combined with revised MM5 Monin-Obukhov scheme were implemented to describe the land-atmosphere exchange (Jiménez et al., 2012; Tewari et al., 2016). The diurnal variation of planetary boundary layer (PBL) was represented by Yonsei University PBL scheme under the influence of dust as well as anthropogenic aerosols (Hong et al., 2006). For numerical characterization of atmospheric chemistry, the Carbon Bond Mechanism version Z gas-phase chemistry and Model for Simulating Aerosol Interactions and Chemistry (MOSAIC) aerosol scheme were adopted (Zaveri & Peters, 1999; Zaveri et al., 2008), in which aerosols were assumed to be spherical particles divided into four discrete bins (0.039–0.156, 0.156–0.625, 0.625–2.5, and 2.5–10 μm) according to their dry diameters. Aerosols were internally mixed in each size bin and their optical properties (extinction coefficient, single-scattering albedo and asymmetry factor) were computed as a function of wavelength based on Mie theory and volume averaged refractive indices.

Anthropogenic emissions from industrial processes, power plants, on-road mobile sources, residential combustion and agricultural activities were derived from MIX Asian emission inventory database (Multiresolution Emission Inventory for China), covering major pollutants such as carbon monoxide (CO), SO_2, nitrogen oxides (NO_x), ammonia (NH_3) and speciated VOCs with the finest resolution of 0.25° × 0.25° over eastern Asia (M. Li, Zhang, et al., 2017). MEGAN (Model of Emissions of Gases and Aerosols from Nature, version2) module embedded in WRF-Chem is used to calculate biogenic emissions online (Guenther

et al., 2006). More than 20 biogenic species, including isoprene, monoterpenes and sesquiterpenes, were considered and then involved in the photochemistry calculation.

Goddard Chemistry Aerosol Radiation and Transport (GOCART) module coupled with MOSAIC was applied in this study to describe dust emissions based on erosion map and surface wind speed (Ginoux et al., 2001; Zhao et al., 2010). To be specific, the dust emission flux could be estimated by the expression:

$$F_p = CSs_p U_{10m}^2 \left(U_{10m} - U_t\right), \quad U_{10m} > U_t$$

where p represents the particle size range, and C is a dimensional factor could be valued as 1 μg s^2 m^{-5}; S denotes the source function derived from soil erodibility by wind; s_p is the fraction of each size range in erodible dust, including clay, silt and sand which are in different size bins. Dynamic variables are U_{10m} (horizontal wind speed at 10 m) from meteorological fields and U_t (threshold velocity) depending on particle size and soil moisture (Fécan et al., 1999; Shao & Lu, 2000).

Mineral dust can impact the transfer of radiation through both scattering and absorption. However, the refractive index of dust has always been controversial. For shortwave radiation, the real part of the refractive index for dust was well acknowledged and set to 1.53 in the model, while the imaginary part, which stands for its absorptivity, varies a lot. Observations over east and central Asia identified the imaginary values to be 0.0022 for pure dust and 0.0036 for transported polluted dust (Bi et al., 2016). Laboratory study also showed quite a large range from 0.0006 to 0.0048 at 520 nm for dust from eight different source regions. A recommended value of 0.003 was selected to perform the simulation (Zhao et al., 2010). For longwave radiation, refractive index is strongly dependent on wavelength, and values from Optical Properties of Aerosols and Clouds data set were employed (Hess et al., 1998).

Two parallel simulations are designed: one without aerosol's effect (noARI), in which the aerosols cannot perturb radiation transfer and cloud microphysical processes, and one with interactions between aerosols and meteorological fields (ARI), in which optical properties of aerosols were calculated at each time step and then coupled with the radiative transfer model for both short- and long-wave radiation to further perturb meteorology. Domain settings and model configurations are exactly the same as aforementioned for the pair of simulations to explore the impact of dust aerosols on radiative energy budget, downwind accumulation of primary pollutions over land and secondary pollution formation over the sea surface.

2.3. Identification of Potential Source Regions

With the intension to identify transport pathways of air masses during the studied episode, the Lagrangian particle dispersion model (LPDM) was operated using Hybrid Single-Particle Lagrangian Integrated Trajectory model for crucial days during the event (A. Ding et al., 2013; Stein et al., 2015). In general, 3,000 particles were released every hour from the receptor at a specific height (100 m) and were then tracked backward for several days. The positioning of particles was determined by mean wind patterns and a turbulent transport component after they are released from the backward starting point. Particle residence times of below 100 m were used to identify the "footprint" retroplume, the spatiotemporal distribution of which were indicative of potential source regions and their relative contributions to air masses at specific locations. Specifically, LPDM model was first performed for Shanghai (31.2°N, 121.43°E) on 2 November to achieve the entire transport pathway of the dust, driven by 1° × 1° Global data assimilation system data, and then for Nanjing (32.05°N, 118.78°E) on October 30 to examine the change of diffusion conditions influenced by aerosols, driven by WRF-Chem output files under noARI/ARI conditions.

3. Results and Discussions

3.1. Mixed Pollution Episode and Model Evaluations

The formation of dust events has usually been related to cold weather systems with high surface wind speed (Husar et al., 2001; J. Kim, 2008). On October 27, 2019, the Mongolia cyclone was located northwest of Gobi Desert and rapidly moved eastward, resulting in cold air invasion behind (Figure S1). Due to a strong baroclinic instability at 850 hPa and corresponding large pressure gradient at surface, the average wind speed

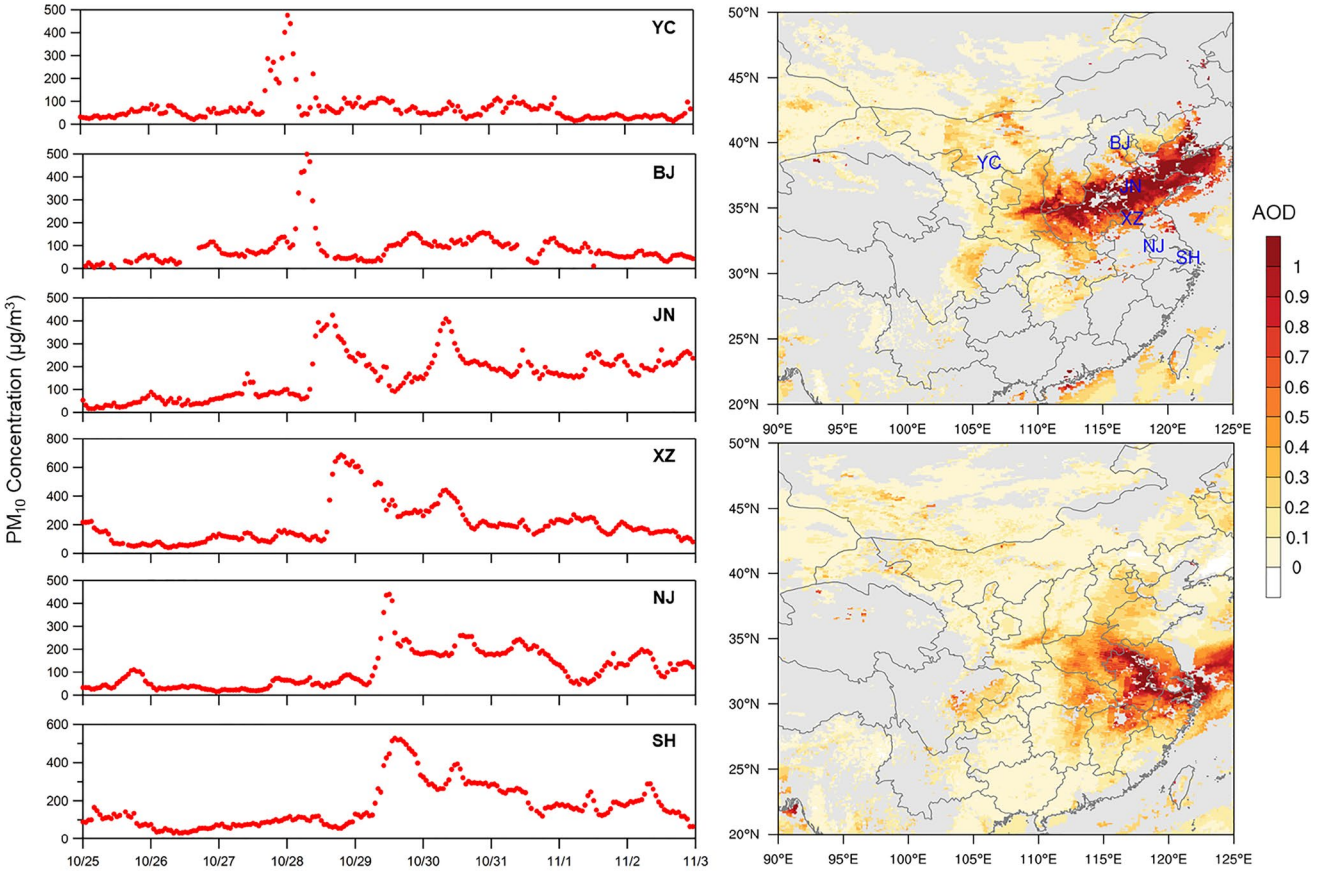

Figure 1. (Left column) Time series of PM_{10} concentrations at different air quality monitoring stations (YC: Yinchuan, BJ: Beijing, JN: Jinan, XZ: Xuzhou, NJ: Nanjing, SH: Shanghai) during the dust episode. The corresponding locations of these stations are marked in blue on the right map. (Right column) Aerosol optical depth at 550 nm over eastern China retrieved by MODIS satellite on 28 (upper) and 29 (lower) October. Missing values are shaded in gray. MODIS, MODerate resolution Imaging Spectroradiometer.

over Gobi reached as high as 15 m/s, which was well above generally assumed threshold wind speed (9 m/s) for Asian dust suspension (Kurosaki & Mikami, 2007). Combined with extremely low relative humidity (RH, ~20%), the dust storm broke out in the afternoon of 27 October and swept through most part of China, including northeast China, North China Plain (NCP), and YRD areas.

According to ground-based measurements and satellite observations, the dust took a southern route from the north to central and eastern China (Figure 1, Figure S2). Situated close to the dust source region, Yinchuan (YC) was greatly affected by the storm with an hourly PM_{10} concentration reaching 500 $\mu g/m^3$ at 00 local time (LT) on 28 October. Highest concentration of mineral dust was detected 6 h later in Beijing (BJ) with a rather sharp peak, indicating the fast moving of the dust plume passing by the city. Station Jinan (JN) and Xuzhou (XZ), located in the center of NCP, showed similar variations, with average coarse particle concentration on the dust outbreak day being 229 and 304 $\mu g/m^3$ respectively. After its arrival at Nanjing and Shanghai within 48 h, the dust plume moved eastward to the ocean surface. The spatial distribution of the dust pollution is also displayed in Figure 1 by satellite retrieved AOD. The dust plume characterized with AOD larger than one moved swiftly from north to south, and then exported to East China Sea at YRD. These features were generally reproduced by our model simulations (Figure S2). Additionally, contemporaneous surface coarse particle concentrations from air quality monitoring stations and regional modeling are also presented in Figure S2, with a more detailed statistical evaluation for both meteorological variables and major pollutants including PM_{10} and ozone for the entire episode (Table S1). The correlation coefficients for atmospheric fundamental variables such as temperature and relative humidity were over 0.8 with mean bias of −0.25°C and −3%, respectively. The predictions of PM_{10} and ozone are also reasonably well with normalized mean bias of 16% and 11%. Possible reasons for bias could be missing or inaccurate model

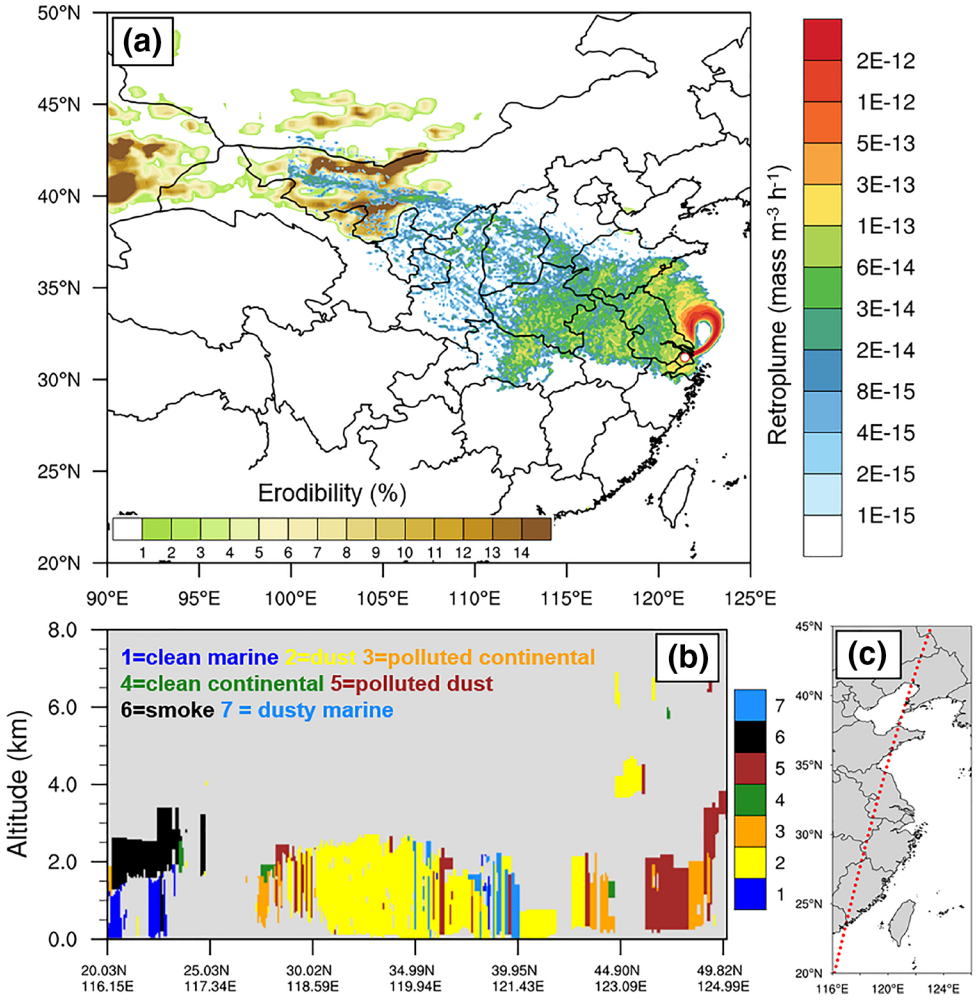

Figure 2. (a) 5-day backward footprint calculated by LPDM initiated on 2 November. Red circle on the map showed the starting point of air masses, Shanghai. The brownish contour represents erodibility of Gobi Desert. (b) and (c) Vertical cross section of aerosol type determined by CALIPSO on 28 October at 18:20 UTC and the corresponding track. LPDM, Lagrangian particle dispersion model; CALIPSO, Cloud-Aerosol Lidar and Infrared Pathfinder Satellite Observation.

representations of subgrid processes as well as uncertainties in emission inventory (M. Li, Liu, et al., 2017; Thomas et al., 2019; Y. Zhang et al., 2016). Despite some deviations, the simulated meteorology and chemical fields show good agreement with observations, which provides a solid foundation for utilizing the simulation results to analyze the episode.

The vertical distribution of the dust plume can be illustrated more clearly by the satellite lidar on board the CALIPSO (Figure 2). A layer of mineral dust over NCP, extending south to YRD city clusters (about 30°N), was primarily located below 2 km in altitude. The extinction of these aerosols is clearly revealed by CALIPSO aerosol profile and well captured by the model (Figure S3). After transported to YRD city clusters, dust aerosol was mixed with anthropogenic pollutants emitted from the ground surface, and was then carried to ocean areas to the east (Figure S4). To gain more general insight into the mixing, the spatial distributions of PM_{10}, representing the dust aerosol, and CO, corresponding to anthropogenic emission are shown in Figure 3. As illustrated by the simulation, the mixed plume (PM_{10} > 400 μg/m^3, CO > 200 ppb) mainly concentrated within PBL, which coincides with satellite retrieval of polluted dust. Five-day backward Lagrangian dispersion simulation was performed on 2 November to acquire the footprint retroplume. The air mass originated from Gobi Desert where the erodibility was greater than 10%, was transported to YRD region and mixed with anthropogenic pollutants on 29–30 October, raising PM_{10} concentrations in urban areas to over 350 μg/m^3. The mixed plume

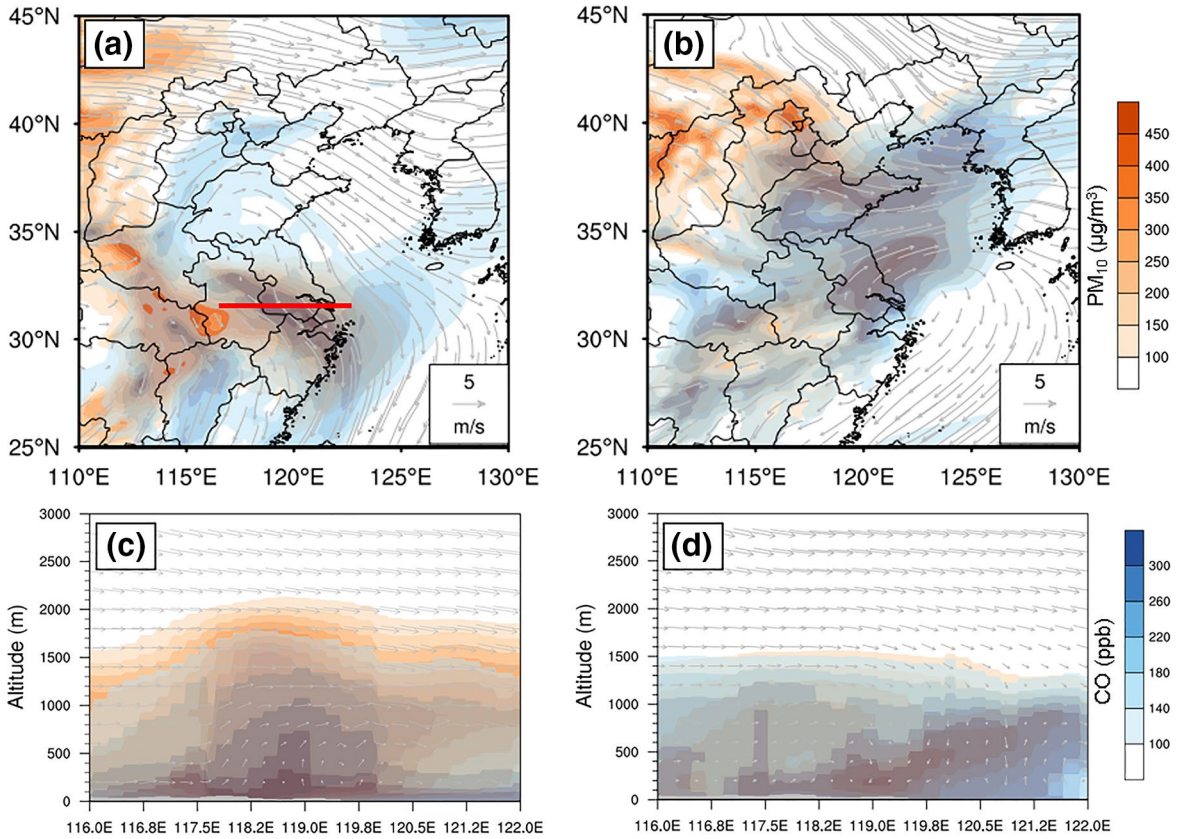

Figure 3. Daily average simulated distribution of dust (PM_{10}) and anthropogenic pollutants (CO) on (a) 29 and (b) 31 October at the altitude of 500 m. Vectors show synoptic circulations. Vertical cross section of PM_{10} and CO through YRD region and zonal wind (share the same reference vector with (a)) on (c) 29 and (d) 31 October. The position of the cross section is marked by the red line on the first map. YRD, Yangtze River Delta.

was then exported to the East China Sea before recirculated back to YRD on 2 November, accompanied by enhanced secondary pollution. The hourly secondary inorganic aerosols reached over 100 μg/m^3 and maximum daily 8-h average (MDA8) ozone increased to 80 ppb (Figure 4 and Figure S5). The composition and formation mechanism of these two pollution episodes in YRD city clusters are quite different and will be studied separately in the following sections.

3.2. Dust-Induced Feedback Intensifying the Pollution Accumulation

As the dust plume passed through, a quick transformation of atmospheric aerosol composition took place in Nanjing (Figure 4). The coarse particles experienced an abrupt increase to over 500 μg/m^3 in the afternoon of 29 October, in consistence with Calcium, which is the main ingredient of mineral aerosols. By comparison, the secondary aerosols including nitrate, sulfate, and ammonium declined from 60 to less than 20 μg/m^3, due mainly to horizontal dispersion caused by large wind speed (exceeding 5 m/s) associated with frontal system. Simultaneously, surface observed incoming shortwave radiation was greatly diminished, the maximum of which is only 621 W/m^2 compared to 700 W/m^2 the day before, both under clear sky condition. The reduction can be attributed to the extinction of dust mixed with other anthropogenic aerosols, which is also verified by the discrepancies between ARI and noARI simulations, namely a 70 W/m^2 decrease in solar radiation on 29 October (Figure S6). Generally, the average daytime shortwave radiation is 440 W/m^2 in noARI scenario but declines to 370 W/m^2 considering the effect of aerosol during the episode, the latter of which is closer to the observed 369 W/m^2.

However, due to the absorption of dust aerosols, it aroused not only a negative radiative forcing at the earth surface, but also a positive forcing within the atmosphere (J. Huang et al., 2014; L. Liu et al., 2016). Near surface cooling caused by less energized underlying surface and atmospheric warming induced by dust

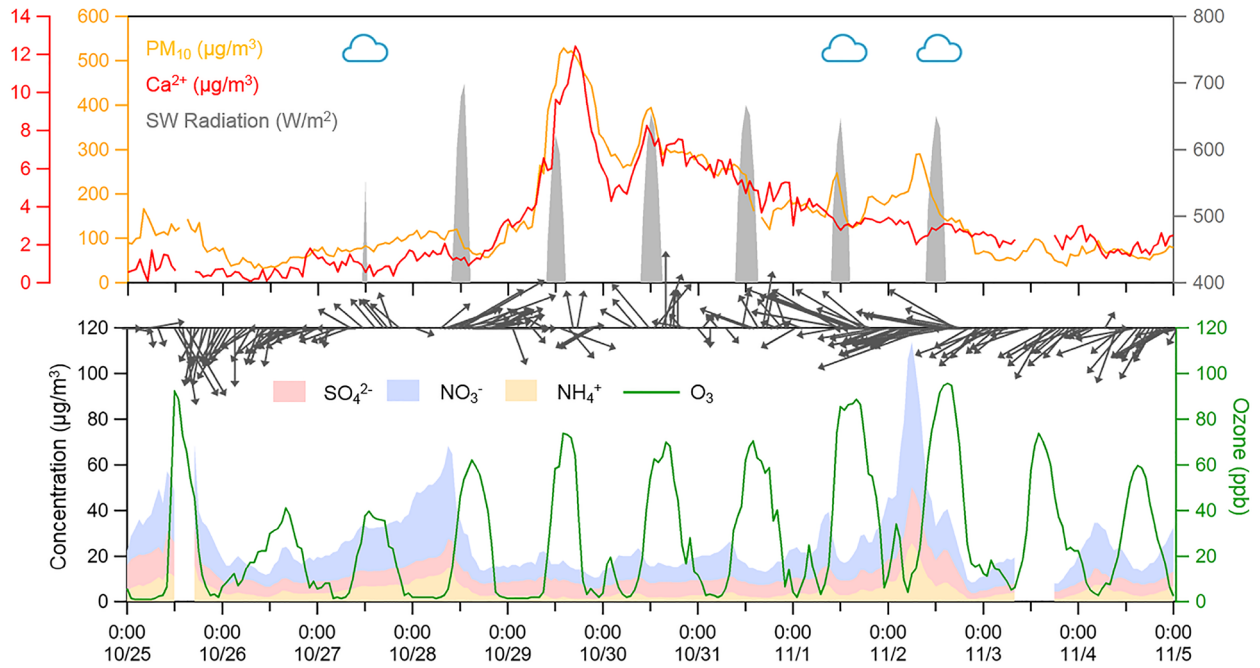

Figure 4. Time series of incoming shortwave radiation, PM_{10} and calcium concentration along with secondary pollution including inorganic aerosols (sulfate, nitrate, and ammonium) and ozone observed at SORPES in Nanjing during the pollution episode. Cloudy days are marked with blue cloud icon at the top.

heating were clearly demonstrated as in Figure 5. On 29 October, a maximum warming of 0.3°C was concentrated between 1.5 and 2 km with little diurnal variation, suggesting a large-scale transported heating dust layer. After mixed with locally emitted pollutants, the mixed plume aroused a more intensive feedback pattern on 30 October at Nanjing, increasing the upper level warming to 0.5°C. The surface cooling lasted through the entire dust episode despite some offset by the entrainment of warmed air into PBL in the late morning (Z. Wang, Huang, & Ding, 2018). Such variations of stratification were also confirmed by sounding observations. Since the global forecast system has not considered the effect of aerosols on meteorology yet, the disparities between atmospheric sounding observations and forecast temperature profile could reflect the impact exerted by aerosols to some extent. In order to avoid deviation caused by strong synoptic process, temperature profiles from 30 October instead of 29 were studied. The vertical air temperature detected by radiosonde displayed a significant positive bias relative to the forecast at upper levels while negative in lower atmosphere at both 00 (08) and 12 (20) UTC (Local Time). Therefore, upper level warming combined with surface cooling generated a more stabilized boundary layer, and also denoted the vertical redistribution of solar energy. In comparison, temperature profiles from WRF-Chem simulations show similar pattern due to the assimilation of observation in initial conditions from NCEP, yet ARI exhibits more atmospheric heating and closer to observations (Figure S7). The diurnal variations of PBL height with and without the aerosol's feedback are shown as well. The tardive evolvement in the morning, the advanced fall in the afternoon and the overall shallower mixing height (1,125 m/1,309 m in feedback/no-feedback situation) due to dust-induced ARI are consistent with previous modeling and observational studies (A. J. Ding et al., 2016; X. Huang et al., 2018).

With stabilized stratification in the lower troposphere, the concentration of surface pollutants changed as a response. Figure 6 shows the spatial distribution of PM_{10} as well as perturbations of daytime PBL height and surface concentration of primary pollutants. The daytime average coarse particles reached a maximal concentration of 450 $\mu g/m^3$ at the west of YRD, with the high value center located in Nanjing. Correspondingly, the reduction of PBL height induced by aerosol-radiation feedback exceeded 150 m at the center of the pollution belt, greatly hindering the diffusion and dispersion of near surface pollutants. The concentration of near surface CO, which is the primary pollutant mainly caused by anthropogenic emissions in urban areas, increased by about 50 ppb (~10%). This increment resulted from both weakened vertical mixing and reduced horizontal dispersion, the latter being clearly demonstrated as in Figure 7. Under the influence

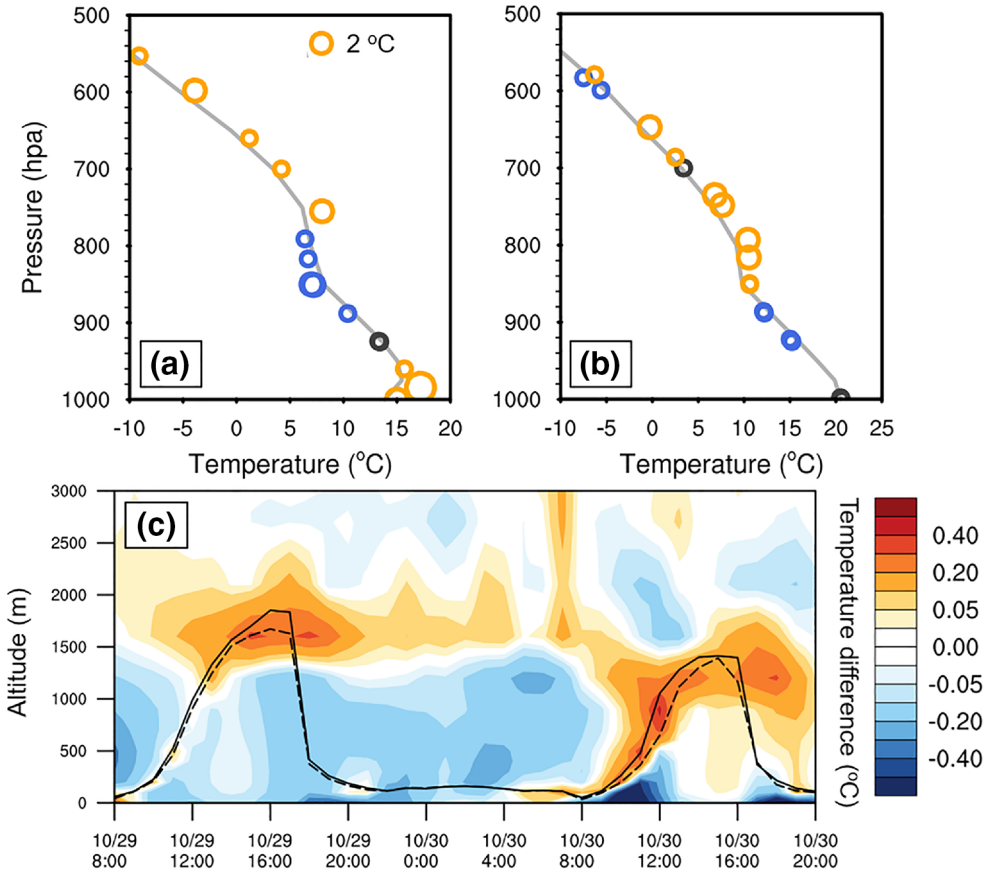

Figure 5. Atmospheric sounding of air temperature (circles) compared with its counterpart in GFS (gray line) at (a) 00 and (b) 12 UTC on 30 October at Nanjing. Orange circle denotes positive bias (observation greater than forecast), while blue circle negative. The relative size of the circle represents absolute value of bias. (c) Temperature difference at Nanjing caused by ARI in WRF-Chem simulation and PBL height in two scenarios (solid line for noARI and dash line for ARI). ARI, aerosol-radiation interaction; GFS, global forecast system.

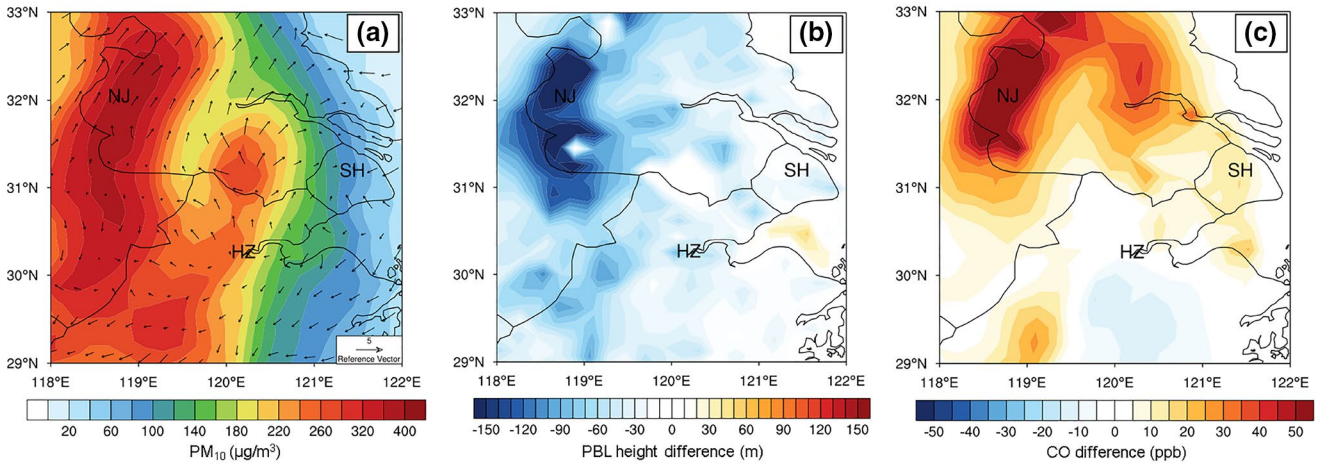

Figure 6. (a) Spatial distribution of PM_{10} concentration and surface wind fields on 30 October. (b) The reduction of daytime PBL height and (c) the enhancement of near-surface CO concentration caused by aerosol-radiation feedback on 30 October. Three main cities of YRD (SH: Shanghai, NJ: Nanjing, HZ: Hangzhou) are marked on the map. YRD, Yangtze River Delta.

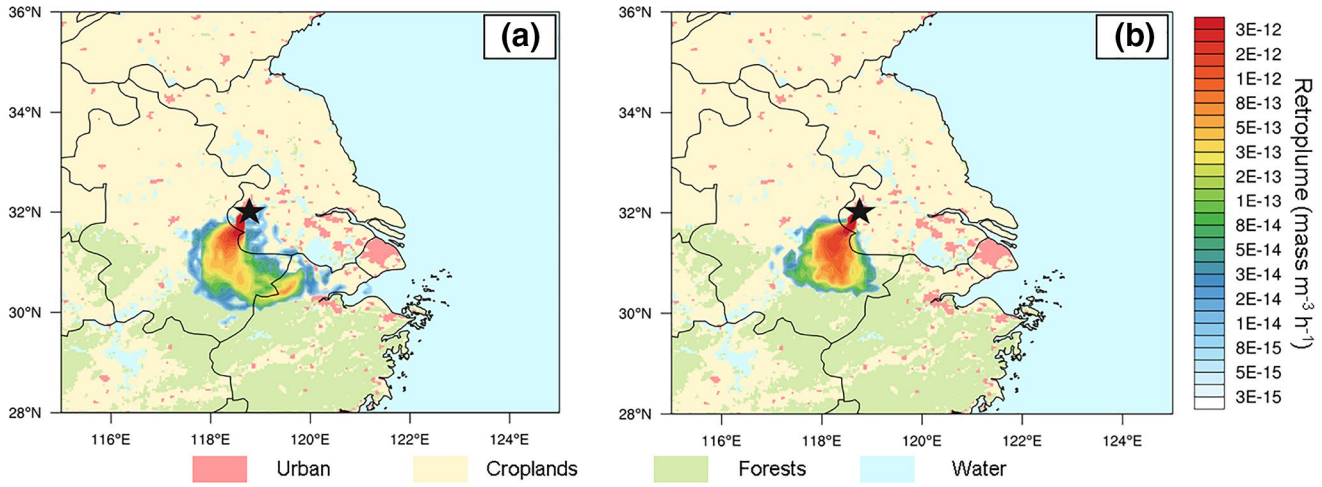

Figure 7. 24-h backward footprint of air mass arriving Nanjing on 30 October calculated by Lagrangian Particle Dispersion Model (LPDM) driven by meteorological fields (a) without and (b) with ARI considered superimposed over the land use map of YRD. Black star on the map shows the location of the starting point Nanjing. ARI, aerosol-radiation interaction; YRD, Yangtze River Delta.

of aerosol-boundary layer meteorology feedback, the scope of 24-h backward footprint originated from Nanjing shrunk significantly, suggesting a poorer ventilation condition for the region.

3.3. Dust-Induced Feedback Enhancing Secondary Pollutants Formation

Absorbing aerosols such as dust could interact with radiation not only over land but also over the ocean. On 2 November, dust aerosols carried by an anticyclonic circulation engulfed most part of eastern China as well as East China Sea, resulting in over 150 μg/m^3 of PM_{10} extending from the surface to 1,000 m above sea level (Figure 8). However, it is noticeable that different and even opposite feedback was triggered over these two surfaces. For the land surface, the cooling effect of all the aerosols dominated with a maximum temperature reduction of more than 1°C at near surface layer and a 0.5°C warming at the altitude of about 1,000 m. On the contrary, the mixed plume over offshore areas east to YRD exhibited a uniformly warming throughout the lower troposphere, that is, 0–500 m above the sea level, accompanied by a negligible effect at higher elevation. Such different variations of atmospheric stratification could be attributed to distinct thermal characteristics of terrestrial fields and the ocean (Q. Ding, Sun, et al., 2019). To be specific, with greater heat capacity, the ocean is less susceptible to the diminution of solar radiation reaching its surface, allowing the warming of the atmosphere caused by absorbing aerosols in charge of the stratification change. Vertically, the atmospheric heating caused by absorbing aerosols located mostly at upper PBL over land surface (Z. Wang, Huang, & Ding, 2018), while the warming over the sea was confined within a less-developed marine boundary layer.

The alteration of humidity conditions due to ARI is also studied. Overall, the latent heat over offshore areas east to YRD was reinforced by about 10 W/m^2 during the daytime, indicative of more evaporation. To investigate the factors contributing to such change, a bulk aerodynamic relationship for moisture flux (proportional to latent heat) over water surface is adopted:

$$F_{\text{water}} = C|U|\left(q_{\text{sat}}(T) - q\right)$$

where C is a dimensionless bulk transfer coefficient for moisture, U is the horizontal wind speed, q_{sat} is the saturated specific humidity at near-surface air temperature T defined by Clausius-Clapeyron equation. Therefore, the difference caused by atmospheric warming and circulation change can be acquired by:

$$\Delta F_{\text{water}} = C|U_1|\left(q_{\text{sat}}(T_1) - q_0\right) - C|U_0|\left(q_{\text{sat}}(T_0) - q_0\right)$$

where subscript 1 denotes situation with ARI while subscript 0 noARI. As near-surface air gets warmer over ocean, the saturated water vapor increases ($q_{\text{sta}}(T_1) > q_{\text{sta}}(T_0)$). Along with greater wind speed ($U_1 > U_0$,

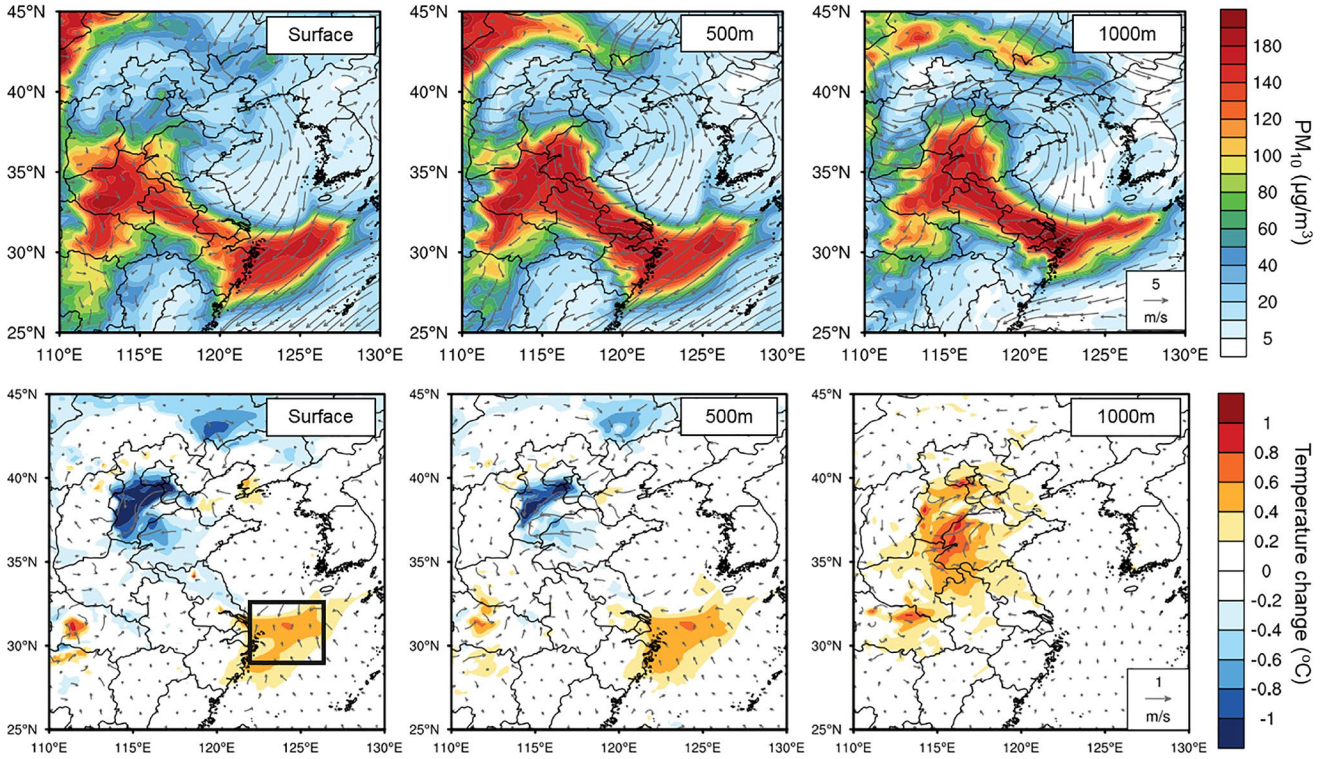

Figure 8. Simulated daytime average PM_{10} (upper panel) and temperature perturbation (lower panel) due to aerosol radiative effect at surface, 500 and 1000 m on 2 November. The area inside the black box with most significant warming is of interest and is the scope of profile average in Figure 10.

Figure 9a), the evaporation is enhanced and the latent heat flux increases. With more evaporation, the RH over ocean in near surface layer increased from 68% to 72% and the water vapor mixing ratio was enhanced by a magnitude of 0.4 g/kg as well. Notably, compared with latent heat perturbation, which well-displayed local surface features, the spatial distribution of RH change took on more homogeneous characteristics due to atmospheric transport and mixing.

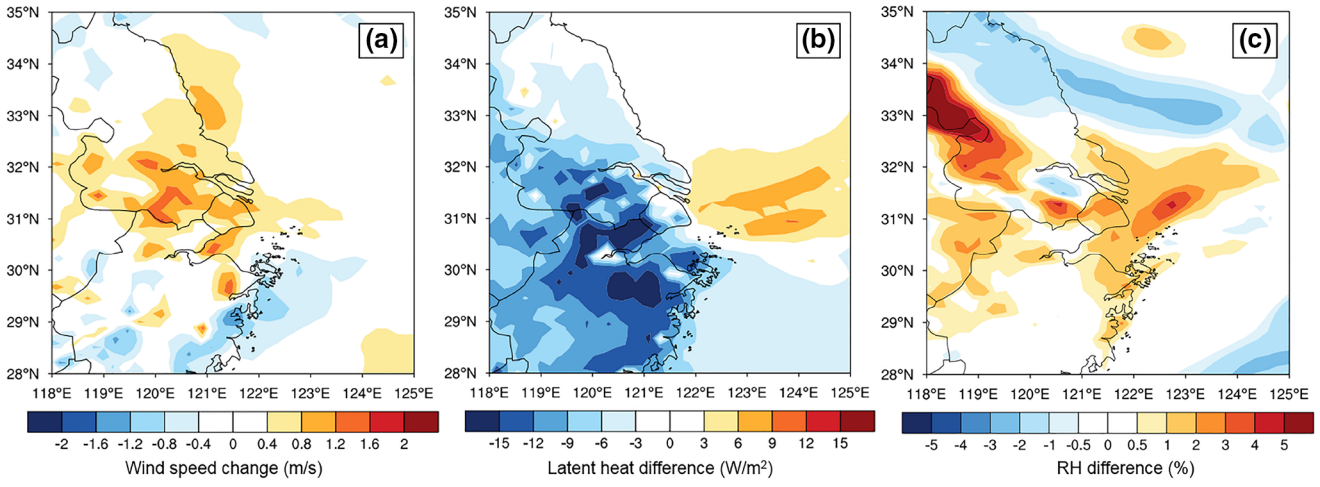

Figure 9. Daytime 10 m wind speed (a), surface latent heat (b), and near surface relative humidity (c) difference between ARI and noARI scenario on 2 November around YRD region. ARI, aerosol-radiation interaction; YRD, Yangtze River Delta.

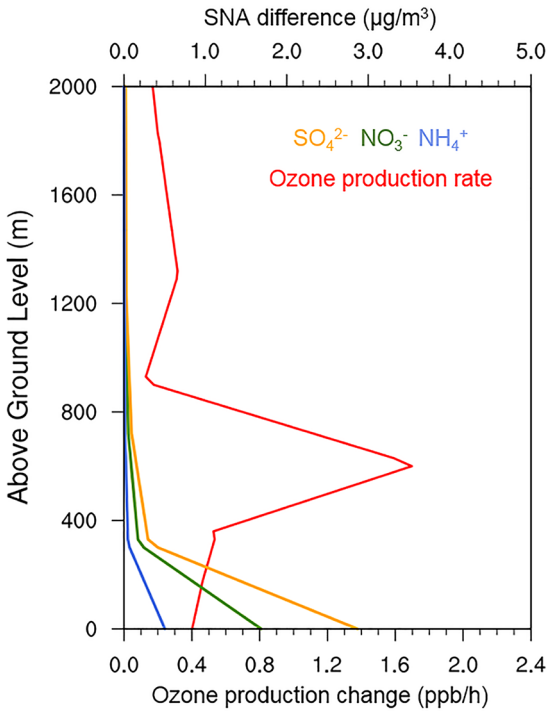

Figure 10. Area-averaged vertical profile of ozone production change and SNA difference caused by aerosol-induced feedback. The area scope is denoted by the black box in Figure 8. SNA, sulfate, nitrate, and ammonium.

Under warm and humid environments, air mass containing anthropogenic gas precursors is conducive to form secondary pollution including ozone and inorganic aerosols. Higher temperature could promote ozone production through several ways. First, the absorption cross-section of ozone, which is proportional to photolysis frequency of the gas, increased with temperature (Chehade et al., 2013), indicating a positive correlation of air temperature and photochemical reactions. Second, warmer atmosphere triggered faster thermal decomposition of Peroxyacetyl nitrate (PAN), which led to ozone destruction in urban areas yet facilitated ozone formation in remote troposphere due to nonlinear relationship of NO_x (=NO + NO_2) and ozone (Fischer et al., 2014; X. Huang, Ding, Gao, et al., 2020; Singh & Hanst, 1981). Further, overall faster chemical reactions took place under higher temperature. Since that biogenic VOCs (BVOC) emission is generally very small above the ocean, the influence of temperature on BVOC could be omitted. With a notable warming within the boundary layer, the ozone production rate was enhanced by 1 ppbv/h shown in Figure 10 (P. Liu et al., 2020; H. Zhang et al., 2015), which is comparable to the rate of ozone changed with increasing temperature from observations (2.15 ppbv/°C) as well as simulations (2.05 ppbv/°C) (Coates et al., 2016). Higher oxidation rate due to elevated ozone resulted in additional sulfate and nitrate by gas-phase reactions with more OH radical during daylight (Seinfeld, 2006). Besides, moister condition featured larger RH is conducive to heterogeneous reactions that produce more secondary transformation (X. Huang, Ding, Wang, et al., 2020; Sun et al., 2014). As a result, secondary inorganic aerosols, like sulfate, nitrate, and ammonium within the boundary layer substantially increased. Aside from chemical reactions, sufficient water vapor also favors the hygroscopic growth of secondary aerosols. Such process efficiently contributes to ambient particle concentrations as well.

Due to the easterly wind, the mixed plume was finally transported back to coastal cities in YRD such as Shanghai. Surface ozone diagnostic analysis of Shanghai on 2 November is shown in Figure 11. With excessive NO_x emissions from traffic in the city, the chemical processes of ozone were mostly negative due to NO_x titration. By contrast, the most significant contributions of surface ozone resulted from horizontal advection and vertical mixing, indicating the secondary pollution generated over marine surface has a great impact on air quality of seaside cities. To be specific, the ozone concentration remained quite high (~80 ppb)

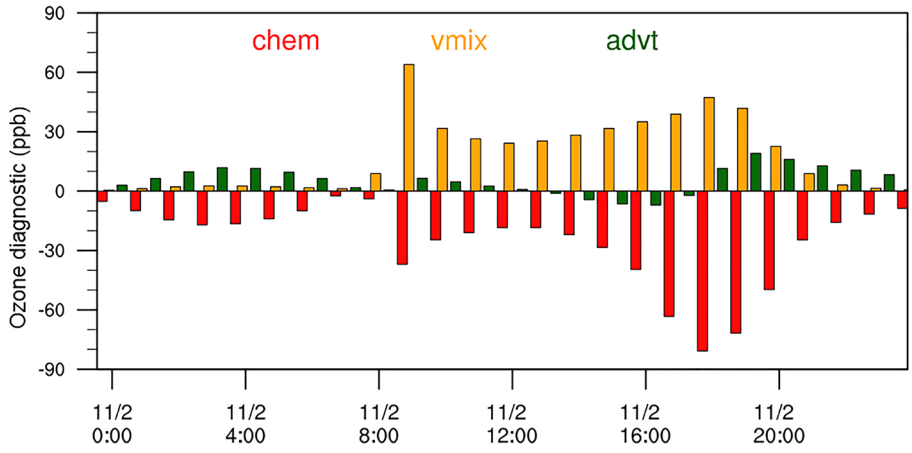

Figure 11. Time series of surface ozone diagnostic analysis (chem: chemical transformation; vmix: vertical mixing; advt: atmospheric advection) at Shanghai on 2 November.

Table 2
Observed MDA8 and Fine Particulate Concentration Compared With Simulations With/Without Aerosol-Radiation Interactions

Average concentration	OBS	ARI	noARI
$PM_{2.5}$ ($\mu g/m^3$)	58.55	49.40	40.04
MDA8 (ppb)	79.04	67.12	54.48

Abbreviation: ARI, aerosol-radiation interaction.

during the daytime on 2 November, suggesting a high atmospheric oxidation capacity. The sulfur oxidation ratio ($SOR = SO_4^{2-} / \left(SO_4^{2-} + SO_2\right)$, all in molar concentration, the same hereafter) and nitrogen oxidation ratio ($\left(NOR = NO_3^- / \left(NO_3^- + NO_2\right)\right)$ increased from 0.20 to 0.32 and 0.07 to 0.16, respectively, suggesting growing secondary aerosols and thus facilitated the particulate matter level enhancement. With the effect of ARI considered, the simulated ozone and fine particle increased by about 20% and 15%, respectively, agreeing better with observations (Table 2). However, underestimations still exist. One possible reason is related to the underrepresented absorption of polluted Asian dust, the single scattering albedo (SSA) of which can reach as low as 0.76, much smaller than generally acknowledged value of 0.9 (Costa et al., 2006; D. H. Kim, 2005). As indicated by underestimation of aerosol extinction (Figure S3) and solar radiation reduction (Figure S6), the extinction of aerosols can be estimated low in the model. Hence, the radiative forcing and its interactions with ambient meteorological conditions can be biased low.

4. Conclusions

On the basis of multiple observations and a coupled atmospheric dynamic model, a widespread dust storm occurring in the autumn of 2019 and its influence on the air quality of downwind cities were investigated comprehensively. Both optical properties and radiative effect of aerosols in this episode were reproduced reasonably well by online-coupled WRF-Chem model. The dust originated from Gobi Desert made its way south under the control of a weak cold front. After transported to YRD region, the dust was mixed with anthropogenic pollutants. Large amount of incoming solar irradiance was scattered as well as absorbed by the aerosol layer, leading to a large-scale surface cooling and upper-level atmospheric heating. Such a stratification change was confirmed by both radiosonde observations and simulations. Owing to more stabilized lower troposphere, a reduction of 15% in averaged daytime (12:00–16:00) PBL height (184 m) was diagnosed, as well as weakened vertical and horizontal dispersion of locally emitted pollutants shown by LPDM model results. Poor ventilation contributed to the degradation of near surface air quality and increased primary pollutants by 10% in YRD city clusters.

After exported to offshore areas, the mixed plume caused quite different aerosol-meteorology feedback compared to continental fields. Instead of surface cooling, an entire lower atmospheric heating occupied the offshore areas east to YRD region with a maximum warming of 0.5°C. In addition, the evaporation and hence relative humidity over the area were enhanced by elevated temperature and larger wind speed. Accordingly, ozone formation was accelerated by ~1 ppbv/h within PBL under higher temperature, and secondary aerosols including sulfate, nitrate, and ammonium increased due to faster photochemical and heterogeneous oxidation. The mixed plume subsequently returned to YRD city clusters with SOR/NOR being amplified by 1.5–2 times, and significantly contributed to the secondary gas and aerosol pollution in seaside cities such as Shanghai. This study reveals the complexity of interactions between natural dust and anthropogenic pollutants through both atmospheric chemistry and meteorological feedbacks, which is of great importance in both regional air pollution and climate.

Data Availability Statement

This work was supported by the National Natural Science Foundation of China (41922038, 91744311, 41725020, and 41875150) and Jiangsu Provincial Fund on PM2.5 and O3 pollution mitigation (2019023). The in situ observed hourly data for chemical species including PM10 from multiple stations and aerosol component at SORPES can be accessed through http://doi.org/10.5281/zenodo.4265503. The radiosonde observations are archived at http://weather.uwyo.edu/upperair/sounding.html, and the global hourly surface meteorological data are available at https://www.ncei.noaa.gov/data/global-hourly/access/. The MODIS daily AOD with a spatial resolution of 10 km can be ordered at https://ladsweb.modaps.eosdis.nasa.gov/search/. The CALIPSO data are available at https://subset.larc.nasa.gov/calipso. The MIX Asian anthropogenic emission inventory is acquired from http://www.meicmodel.org/.

Acknowledgments
This work was supported by the National Natural Science Foundation of China (41922038, 91744311, 41725020, and 41875150). We thank Dr. Qingyan Fu at Shanghai Environmental Monitoring Center for useful discussions.

References

Berge, E., Huang, H.-C., Chang, J., & Liu, T.-H. (2001). A study of the importance of initial conditions for photochemical oxidant modeling. *Journal of Geophysical Research*, *106*(D1), 1347–1363. https://doi.org/10.1029/2000jd900227

Bi, J., Huang, J., Holben, B., & Zhang, G. (2016). Comparison of key absorption and optical properties between pure and transported anthropogenic dust over East and Central Asia. *Atmospheric Chemistry and Physics*, *16*(24), 15501–15516. https://doi.org/10.5194/acp-16-15501-2016

Chehade, W., Gür, B., Spietz, P., Gorshelev, V., Serdyuchenko, A., Burrows, J. P., & Weber, M. (2013). Temperature dependent ozone absorption cross section spectra measured with the GOME-2 FM3 spectrometer and first application in satellite retrievals. *Atmospheric Measurement Techniques*, *6*(7), 1623–1632. https://doi.org/10.5194/amt-6-1623-2013

Chun, Y., Boo, K.-O., Kim, J., Park, S.-U., & Lee, M. (2001). Synopsis, transport, and physical characteristics of Asian dust in Korea. *Journal of Geophysical Research*, *106*(D16), 18461–18469. https://doi.org/10.1029/2001jd900184

Coates, J., Mar, K. A., Ojha, N., & Butler, T. M. (2016). The influence of temperature on ozone production under varying NOx conditions—A modelling study. *Atmospheric Chemistry and Physics*, *16*(18), 11601–11615. https://doi.org/10.5194/acp-16-11601-2016

Costa, M. J., atilde Sohn, B.-J., Levizzani, V., & Silva, A. M. (2006). Radiative forcing of Asian dust determined from the synergized GOME and GMS satellite data—A case study. *Journal of the Meteorological Society of Japan. Ser. II*, *84*(1), 85–95. https://doi.org/10.2151/jmsj.84.85

Ding, A., Huang, X., Nie, W., Chi, X., Xu, Z., Zheng, L., et al. (2019). Significant reduction of PM2.5 in eastern China due to regional-scale emission control: Evidence from SORPES in 2011–2018. *Atmospheric Chemistry and Physics*, *19*(18), 11791–11801. https://doi.org/10.5194/acp-19-11791-2019

Ding, A. J., Huang, X., Nie, W., Sun, J. N., Kerminen, V. M., Petäjä, T., et al. (2016). Enhanced haze pollution by black carbon in megacities in China. *Geophysical Research Letters*, *43*(6), 2873–2879. https://doi.org/10.1002/2016gl067745

Ding, Q., Sun, J., Huang, X., Ding, A., Zou, J., Yang, X., & Fu, C. (2019). Impacts of black carbon on the formation of advection–radiation fog during a haze pollution episode in eastern China. *Atmospheric Chemistry and Physics*, *19*(11), 7759–7774. https://doi.org/10.5194/acp-19-7759-2019

Ding, A., Wang, T., & Fu, C. (2013). Transport characteristics and origins of carbon monoxide and ozone in Hong Kong, South China. *Journal of Geophysical Research: Atmospheres*, *118*(16), 9475–9488. https://doi.org/10.1002/jgrd.50714

Fécan, F., Marticorena, B., & Bergametti, G. (1999). Parametrization of the increase of the aeolian erosion threshold wind friction velocity due to soil moisture for arid and semi-arid areas. Annales Geophysicae, 17(1), 149–157. https://doi.org/10.1007/s00585-999-0149-7Fischer, E. V., Jacob, D. J., Yantosca, R. M., Sulprizio, M. P., Millet, D. B., Mao, J., et al. (2014). Atmospheric peroxyacetyl nitrate (PAN): A global budget and source attribution. *Atmospheric Chemistry and Physics*, *14*(5), 2679–2698. https://doi.org/10.5194/acp-14-2679-2014

Fu, Q., Zhuang, G., Wang, J., Xu, C., Huang, K., Li, J., et al. (2008). Mechanism of formation of the heaviest pollution episode ever recorded in the Yangtze River Delta, China. *Atmospheric Environment*, *42*(9), 2023–2036. https://doi.org/10.1016/j.atmosenv.2007.12.002

Ginoux, P., Chin, M., Tegen, I., Prospero, J. M., Holben, B., Dubovik, O., & Lin, S.-J. (2001). Sources and distributions of dust aerosols simulated with the GOCART model. *Journal of Geophysical Research: Atmospheres*, *106*(D17), 20255–20273. https://doi.org/10.1029/2000jd000053

Grell, G. A., Peckham, S. E., Schmitz, R., McKeen, S. A., Frost, G., Skamarock, W. C., & Eder, B. (2005). Fully coupled "online" chemistry within the WRF model. *Atmospheric Environment*, *39*(37), 6957–6975. https://doi.org/10.1016/j.atmosenv.2005.04.027

Guenther, A., Karl, T., Harley, P., Wiedinmyer, C., Palmer, P. I., & Geron, C. (2006). Estimates of global terrestrial isoprene emissions using MEGAN (model of emissions of gases and aerosols from nature). *Atmospheric Chemistry and Physics*, *6*(11), 3181–3210. https://doi.org/10.5194/acp-6-3181-2006

Gu, D., Wang, Y., Smeltzer, C., & Liu, Z. (2013). Reduction in NO(x) emission trends over China: Regional and seasonal variations. *Environmental Science & Technology*, *47*(22), 12912–12919. https://doi.org/10.1021/es401727e

Hess, M., Koepke, P., & Schult, I. (1998). Optical properties of aerosols and clouds: The software package OPAC. *Bulletin of the American Meteorological Society*, *79*(5), 831–844. https://doi.org/10.1175/1520-0477(1998)079<0831:opoaac>2.0.co;2

Hong, S.-Y., Noh, Y., & Dudhia, J. (2006). A new vertical diffusion package with an explicit treatment of entrainment processes. *Monthly Weather Review*, *134*(9), 2318–2341. https://doi.org/10.1175/mwr3199.1

Huang, X., Ding, A., Gao, J., Zheng, B., Zhou, D., Qi, X., et al. (2020). Enhanced secondary pollution offset reduction of primary emissions during COVID-19 lockdown in China. *National Science Review*, 1–17. https://doi.org/10.1093/nsr/nwaa137

Huang, X., Ding, A., Liu, L., Liu, Q., Ding, K., Niu, X., et al. (2016). Effects of aerosol–radiation interaction on precipitation during biomass-burning season in East China. *Atmospheric Chemistry and Physics*, *16*(15), 10063–10082. https://doi.org/10.5194/acp-16-10063-2016

Huang, X., Ding, A., Wang, Z., Ding, K., Gao, J., Chai, F., & Fu, C. (2020). Amplified transboundary transport of haze by aerosol–boundary layer interaction in China. *Nature Geoscience*, *13*, 428–434. https://doi.org/10.1038/s41561-020-0583-4

Huang, J., Fu, Q., Su, J., Tang, Q., Minnis, P., Hu, Y., et al. (2009). Taklimakan dust aerosol radiative heating derived from CALIPSO observations using the Fu-Liou radiation model with CERES constraints. *Atmospheric Chemistry and Physics*, *9*(12), 4011–4021. https://doi.org/10.5194/acp-9-4011-2009

Huang, X., Wang, Z., & Ding, A. (2018). Impact of aerosol-PBL interaction on haze pollution: Multiyear observational evidences in north China. *Geophysical Research Letters*, *45*(16), 8596–8603. https://doi.org/10.1029/2018gl079239

Huang, J., Wang, T., Wang, W., Li, Z., & Yan, H. (2014). Climate effects of dust aerosols over East Asian arid and semiarid regions. *Journal of Geophysical Research: Atmospheres*, *119*(19), 11398–11416. https://doi.org/10.1002/2014jd021796

Husar, R. B., Tratt, D. M., Schichtel, B. A., Falke, S. R., Li, F., Jaffe, D., et al. (2001). Asian dust events of April 1998. *Journal of Geophysical Research: Atmospheres*, *106*(D16), 18317–18330. https://doi.org/10.1029/2000jd900788

Iacono, M. J., Delamere, J. S., Mlawer, E. J., Shephard, M. W., Clough, S. A., & Collins, W. D. (2008). Radiative forcing by long-lived greenhouse gases: Calculations with the AER radiative transfer models. *Journal of Geophysical Research*, *113*(D13), 103–110. https://doi.org/10.1029/2008jd009944

Jiménez, P. A., Dudhia, J., González-Rouco, J. F., Navarro, J., Montávez, J. P., & García-Bustamante, E. (2012). A revised scheme for the WRF surface layer formulation. *Monthly Weather Review*, *140*(3), 898–918. https://doi.org/10.1175/mwr-d-11-00056.1

Jordan, C. E., Dibb, J. E., Anderson, B. E., & Fuelberg, H. E. (2003). Uptake of nitrate and sulfate on dust aerosols during TRACE-P. *Journal of Geophysical Research*, *108*(D21), 8817–8826. https://doi.org/10.1029/2002jd003101

Kaufman, Y. J., Koren, I., Remer, L. A., Rosenfeld, D., & Rudich, Y. (2005). The effect of smoke, dust, and pollution aerosol on shallow cloud development over the Atlantic Ocean. *Proceedings of the National Academy of Sciences of the U S A*, *102*(32), 11207–11212. https://doi.org/10.1073/pnas.0505191102

Kim, D.-H., Sohn, B. J., Nakajima, T., & Takamura, T. (2005). Aerosol radiative forcing over east Asia determined from ground-based solar radiation measurements. *Journal of Geophysical Research*, *110*(D10), 22–38. https://doi.org/10.1029/2004jd004678
Kim, J. (2008). Transport routes and source regions of Asian dust observed in Korea during the past 40 years (1965–2004). *Atmospheric Environment*, *42*(19), 4778–4789. https://doi.org/10.1016/j.atmosenv.2008.01.040
Kim, K. H., Jahan, S. A., & Kabir, E. (2013). A review on human health perspective of air pollution with respect to allergies and asthma. *Environment International*, *59*, 41–52. https://doi.org/10.1016/j.envint.2013.05.007
Kurosaki, Y., & Mikami, M. (2007). Threshold wind speed for dust emission in east Asia and its seasonal variations. *Journal of Geophysical Research*, *112*(D17), 202–214. https://doi.org/10.1029/2006jd007988
Li, L., Chen, C. H., Fu, J. S., Huang, C., Streets, D. G., Huang, H. Y., et al. (2011). Air quality and emissions in the Yangtze River Delta, China. *Atmospheric Chemistry and Physics*, *11*(4), 1621–1639. https://doi.org/10.5194/acp-11-1621-2011
Li, M., Liu, H., Geng, G., Hong, C., Liu, F., Song, Y., et al. (2017). Anthropogenic emission inventories in China: A review. *National Science Review*, *4*(6), 834–866. https://doi.org/10.1093/nsr/nwx150
Li, J., Wang, Z., Zhuang, G., Luo, G., Sun, Y., & Wang, Q. (2012). Mixing of Asian mineral dust with anthropogenic pollutants over east Asia: A model case study of a super-duststorm in March 2010. *Atmospheric Chemistry and Physics*, *12*(16), 7591–7607. https://doi.org/10.5194/acp-12-7591-2012
Li, M., Zhang, Q., Kurokawa, J.-i., Woo, J.-H., He, K., Lu, Z., et al. (2017). MIX: A mosaic Asian anthropogenic emission inventory under the international collaboration framework of the MICS-Asia and HTAP. *Atmospheric Chemistry and Physics*, *17*(2), 935–963. https://doi.org/10.5194/acp-17-935-2017
Liu, L., Huang, X., Ding, A., & Fu, C. (2016). Dust-induced radiative feedbacks in north China: A dust storm episode modeling study using WRF-Chem. *Atmospheric Environment*, *129*, 43–54. https://doi.org/10.1016/j.atmosenv.2016.01.019
Liu, P., Song, H., Wang, T., Wang, F., Li, X., Miao, C., & Zhao, H. (2020). Effects of meteorological conditions and anthropogenic precursors on ground-level ozone concentrations in Chinese cities. *Environmental Pollution*, *262*, 114366. https://doi.org/10.1016/j.envpol.2020.114366
Lou, S., Yang, Y., Wang, H., Smith, S. J., Qian, Y., & Rasch, P. J. (2019). Black carbon Amplifies haze over the North China Plain by weakening the east Asian Winter monsoon. *Geophysical Research Letters*, *46*(1), 452–460. https://doi.org/10.1029/2018gl080941
Mahowald, N. M., Baker, A. R., Bergametti, G., Brooks, N., Duce, R. A., Jickells, T. D, et al. (2005). Atmospheric global dust cycle and iron inputs to the ocean. *Global Biogeochemical Cycles*, *19*(4), 25–41. https://doi.org/10.1029/2004gb002402
McKeen, S. A. (2002). Ozone production from Canadian wildfires during June and July of 1995. *Journal of Geophysical Research*, *107*(D14), 4192–4206. https://doi.org/10.1029/2001jd000697
Nie, W., Ding, A., Wang, T., Kerminen, V. M., George, C., Xue, L., et al. (2014). Polluted dust promotes new particle formation and growth. *Scientific Reports*, *4*, 6634. https://doi.org/10.1038/srep06634
Obregón, M. A., Pereira, S., Salgueiro, V., Costa, M. J., Silva, A. M., Serrano, A., & Bortoli, D. (2015). Aerosol radiative effects during two desert dust events in August 2012 over the Southwestern Iberian Peninsula. *Atmospheric Research*, *153*, 404–415. https://doi.org/10.1016/j.atmosres.2014.10.007
Painter, T. H., Barrett, A. P., Landry, C. C., Neff, J. C., Cassidy, M. P., Lawrence, C. R., et al. (2007). Impact of disturbed desert soils on duration of mountain snow cover. *Geophysical Research Letters*, *34*(12), 502–507. https://doi.org/10.1029/2007gl030284
Seinfeld, J. H., & Pandis, S. N. (2006). *Atmospheric chemistry and physics: From air pollution to climate change* (2nd ed. New York, NY:). Wiley.
Shao, Y., & Dong, C. H. (2006). A review on East Asian dust storm climate, modelling and monitoring. *Global and Planetary Change*, *52*(1–4), 1–22. https://doi.org/10.1016/j.gloplacha.2006.02.011
Shao, Y., & Lu, H. (2000). A simple expression for wind erosion threshold friction velocity. *Journal of Geophysical Research*, *105*(D17), 22437–22443. https://doi.org/10.1029/2000jd900304
Shiraiwa, M., Ueda, K., Pozzer, A., Lammel, G., Kampf, C. J., Fushimi, A., et al. (2017). Aerosol health effects from molecular to global scales. *Environmental Science & Technology*, *51*(23), 13545–13567. https://doi.org/10.1021/acs.est.7b04417
Singh, H. B., & Hanst, P. L. (1981). Peroxyacetyl nitrate (PAN) in the unpolluted atmosphere: An important reservoir for nitrogen oxides. *Geophysical Research Letters*, *8*(8), 941–944. https://doi.org/10.1029/GL008i008p00941
Stein, A. F., Draxler, R. R., Rolph, G. D., Stunder, B. J. B., Cohen, M. D., & Ngan, F. (2015). NOAA's HYSPLIT atmospheric transport and dispersion modeling system. *Bulletin of the American Meteorological Society*, *96*(12), 2059–2077. https://doi.org/10.1175/bams-d-14-00110.1
Sun, Y., Jiang, Q., Wang, Z., Fu, P., Li, J., Yang, T., & Yin, Y. (2014). Investigation of the sources and evolution processes of severe haze pollution in Beijing in January 2013. *Journal of Geophysical Research: Atmospheres*, *119*(7), 4380–4398. https://doi.org/10.1002/2014jd021641
Tewari, M., Wang, W., Dudhia, J., LeMone, M. A., Mitchell, K., Ek, M., et al. (2016). Implementation and verification of the united NOAH land surface model in the WRF model. 20th conference on weather analysis and forecasting/16th conference on numerical weather prediction, pp. 11–15.
Thomas, A., Huff, A. K., Hu, X.-M., & Zhang, F. (2019). Quantifying uncertainties of ground-level ozone within WRF-Chem simulations in the mid-Atlantic region of the United States as a response to variability. *Journal of Advances in Modeling Earth Systems*, *11*(4), 1100–1116. https://doi.org/10.1029/2018ms001457
Tian, P., Zhang, L., Ma, J., Tang, K., Xu, L., Wang, Y., et al. (2018). Radiative absorption enhancement of dust mixed with anthropogenic pollution over East Asia. *Atmospheric Chemistry and Physics*, *18*(11), 7815–7825. https://doi.org/10.5194/acp-18-7815-2018
Vinoj, V., Rasch, P. J., Wang, H., Yoon, J.-H., Ma, P.-L., Landu, K., & Singh, B. (2014). Short-term modulation of Indian summer monsoon rainfall by West Asian dust. *Nature Geoscience*, *7*(4), 308–313. https://doi.org/10.1038/ngeo2107
Wang, Q., Dong, X., Fu, J. S., Xu, J., Deng, C., Jiang, Y., et al. (2018). Environmentally dependent dust chemistry of a super Asian dust storm in March 2010: Observation and simulation. *Atmospheric Chemistry and Physics*, *18*(5), 3505–3521. https://doi.org/10.5194/acp-18-3505-2018
Wang, X., Dong, Z., Zhang, J., & Liu, L. (2004). Modern dust storms in China: An overview. *Journal of Arid Environments*, *58*(4), 559–574. https://doi.org/10.1016/j.jaridenv.2003.11.009
Wang, Z., Huang, X., & Ding, A. (2018). Dome effect of black carbon and its key influencing factors: A one-dimensional modelling study. *Atmospheric Chemistry and Physics*, *18*(4), 2821–2834. https://doi.org/10.5194/acp-18-2821-2018
Zaveri, R. A., Easter, R. C., Fast, J. D., & Peters, L. K. (2008). Model for simulating aerosol interactions and chemistry (MOSAIC). *Journal of Geophysical Research*, *113*(D13), 204–232. https://doi.org/10.1029/2007jd008782
Zaveri, R. A., & Peters, L. K. (1999). A new lumped structure photochemical mechanism for large-scale applications. *Journal of Geophysical Research*, *104*(D23), 30387–30415. https://doi.org/10.1029/1999jd900876
Zhang, X.-X., Sharratt, B., Liu, L.-Y., Wang, Z.-F., Pan, X.-L., Lei, J.-Q., et al. (2018). East Asian dust storm in May 2017: Observations, modelling, and its influence on the Asia-Pacific region. *Atmospheric Chemistry and Physics*, *18*(11), 8353–8371. https://doi.org/10.5194/acp-18-8353-2018

Zhang, H., Wang, Y., Hu, J., Ying, Q., & Hu, X. M. (2015). Relationships between meteorological parameters and criteria air pollutants in three megacities in China. *Environmental Research*, *140*, 242–254. https://doi.org/10.1016/j.envres.2015.04.004

Zhang, Y., Zhang, X., Wang, L., Zhang, Q., Duan, F., & He, K. (2016). Application of WRF/chem over east Asia: Part I. Model evaluation and intercomparison with MM5/CMAQ. *Atmospheric Environment*, *124*, 285–300. https://doi.org/10.1016/j.atmosenv.2015.07.022

Zhao, C., Liu, X., Leung, L. R., Johnson, B., McFarlane, S. A., Gustafson, W. I., et al. (2010). The spatial distribution of mineral dust and its shortwave radiative forcing over north Africa: Modeling sensitivities to dust emissions and aerosol size treatments. *Atmospheric Chemistry and Physics*, *10*(18), 8821–8838. https://doi.org/10.5194/acp-10-8821-2010

Zhao, C., Liu, X., Ruby Leung, L., & Hagos, S. (2011). Radiative impact of mineral dust on monsoon precipitation variability over West Africa. *Atmospheric Chemistry and Physics*, *11*(5), 1879–1893. https://doi.org/10.5194/acp-11-1879-2011

Zheng, B., Chevallier, F., Ciais, P., Yin, Y., Deeter, M. N., Worden, H. M., et al. (2018). Rapid decline in carbon monoxide emissions and export from East Asia between years 2005 and 2016. *Environmental Research Letters*, *13*(4), 044007. https://doi.org/10.1088/1748-9326/aab2b3

Zhou, D., Ding, K., Huang, X., Liu, L., Liu, Q., Xu, Z., et al. (2018). Transport, mixing and feedback of dust, biomass burning and anthropogenic pollutants in eastern Asia: A case study. *Atmospheric Chemistry and Physics*, *18*(22), 16345–16361. https://doi.org/10.5194/acp-18-16345-2018